

# RF-3DGS: Wireless Channel Modeling with Radio Radiance Field and 3D Gaussian Splatting

Lihao Zhang, *Student Member, IEEE*, Haijian Sun, *Senior Member, IEEE*, Samuel Berweger, Camillo Gentile, *Member, IEEE*, and Rose Qingyang Hu, *Fellow, IEEE*

**Abstract**—Precisely modeling radio propagation in complex environments has been a significant challenge, especially with the advent of 5G and beyond networks, where managing massive antenna arrays demands more detailed information. Traditional methods, such as empirical models and ray tracing, often fall short, either due to insufficient details or with challenges for real-time applications. Inspired by the newly proposed 3D Gaussian Splatting method in computer vision domain, which outperforms in reconstructing optical radiance fields, we propose RF-3DGS, a novel approach that enables precise site-specific reconstruction of radio radiance fields from sparse samples. RF-3DGS can render spatial spectra at arbitrary positions within 2 ms following a brief 3-minute training period, effectively identifying dominant propagation paths at these locations. Furthermore, RF-3DGS can provide fine-grained Channel State Information (CSI) of these paths, including the angle of departure and delay. Our experiments, calibrated through real-world measurements, demonstrate that RF-3DGS not only significantly improves rendering quality, training speed, and rendering speed compared to state-of-the-art methods but also holds great potential for supporting wireless communication and advanced applications such as Integrated Sensing and Communication (ISAC).

**Index Terms**—Wireless Channel Modeling, 3D Gaussian Splatting, Radio Radiance Field, Digital Twin

## I. INTRODUCTION

### A. Modeling the Radio Propagation

Wireless communication systems facilitate the exchange of information carried by Electromagnetic (EM) waves between physically separated Transmitter (Tx) and Receiver (Rx). As EM waves propagate from the Tx to the Rx, they undergo various interactions, including reflection, diffraction, refraction, and scattering. Consequently, these waves may reach the Rx via multiple paths, each characterized by distinct CSI. Radio propagation modeling, which involves characterizing these propagation paths, has been the focus of extensive research due to its crucial role in the design, assessment, and deployment of radio networks [1].

Over the years, various methods for radio propagation modeling have been developed. The empirical models [2],

[3], [4], [5], although effective for providing coarse-grained path loss information over large distances (from hundreds of meters to tens of kilometers), lack precision. Computational Electromagnetics (CEM) methods [6], [7], while being powerful for small-scale modeling, such as antenna design and near-field communication [8], [9], are impractical for a wider range of applications. As 5G and emerging 6G networks demand higher accuracy and more comprehensive radio propagation modeling, ray tracing offers a potential solution by approximating radio waves using ray concepts [10], [11], [12], [13], [14]. However, ray tracing is still limited by its high computational complexity and stringent environmental data requirements, making it unsuitable for more general and real-time applications.

For modeling radio wave propagation using ray tracing methods, a similar trend has emerged in the Computer Vision (CV) domain for 3D scene reconstruction, where volume rendering techniques [15] are employed based on photographs to optimize scene representations [16], [17], [18], [19], [20], [21]. These representations typically capture the optical radiance emitted from object surfaces towards the camera, thereby enabling novel view synthesis and environment reconstruction. In this process, the radiance field is modeled as rays passing through each pixel to the camera, similar to how wireless channels are modeled by Multi-Path Components (MPCs) identified by their Angles of Arrival (AoA). This similarity suggests that such CV techniques could offer valuable insights for enhancing radio wave propagation modeling.

A pioneering work of them is Neural Radiance Fields (NeRF) [16], which achieves exceptional synthesis quality with very sparse input. NeRF's success is grounded in two key components: differentiable volume rendering and neural radiance representation. Volume rendering visualizes volumetric data by casting rays through pixels and integrating their contributions along the ray to determine each pixel's color. The differentiability of this process enables gradient descent optimization from training images to the neural radiance representation, which consists of a geometry density Multi-Layer Perceptron (MLP) and a radiance feature MLP. Despite its groundbreaking results, NeRF has notable limitations, including long training times (up to tens of hours), slow inference times (several seconds), and its implicit neural network representation, requiring exhaustive querying of the scene to obtain geometric information.

Recently, 3D Gaussian Splatting (3DGS) [22] has emerged as a trendsetter, achieving higher reconstruction quality with significantly reduced training times (tens of minutes) and

L. Zhang and H. Sun (lihao.zhang@uga.edu, hsun@uga.edu) are with the School of Electrical and Computer Engineering, University of Georgia, Athens, GA, 30602 USA.

S. Berweger (samuel.berweger@nist.gov) is with the RF Technology Division, National Institute of Standards and Technology, Boulder, CO, 80305 USA.

C. Gentile (camillo.gentile@nist.gov) is with the Wireless Networks Division, National Institute of Standards and Technology, Gaithersburg, MD, 20899 USA.

R. Q. Hu (rose.hu@usu.edu) is with Department of Electrical and Computer Engineering, Utah State University, Logan, UT, 84341 USA.

Dataset and codes of this paper will be available after paper acceptance.

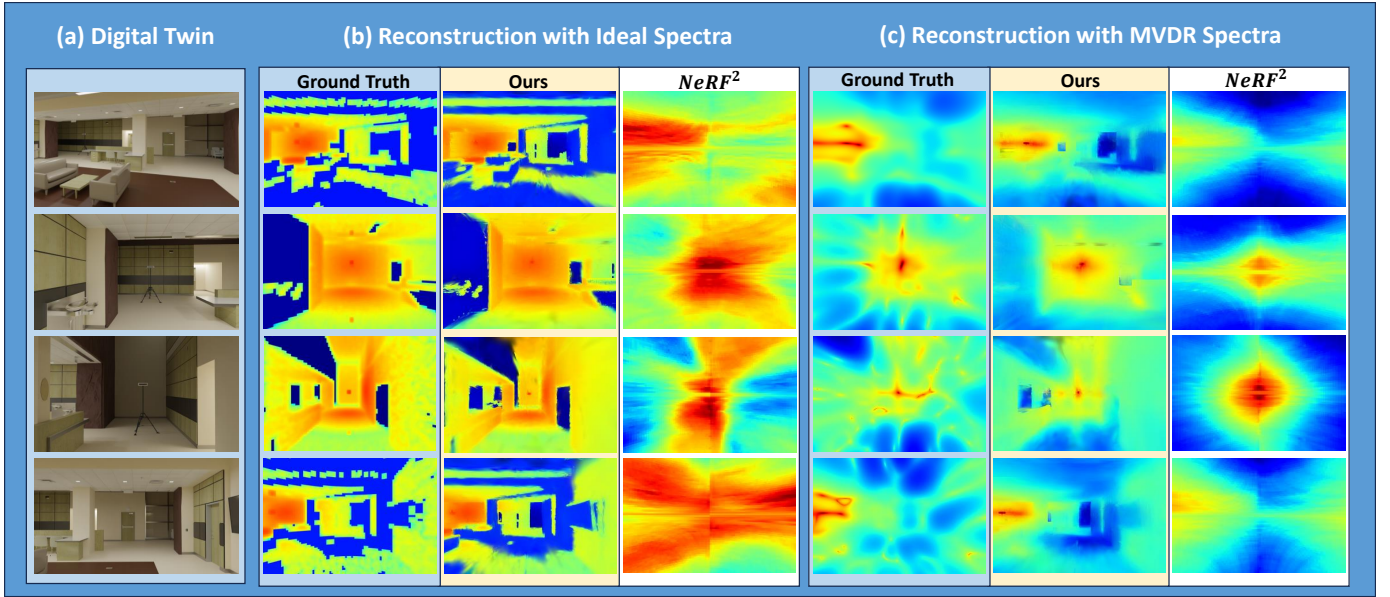


Fig. 1. Reconstructed radio spatial spectra. This figure compares the digital twin, the training ground truth, and the spectra reconstructed by our method and  $NeRF^2$ . (a) shows the digital twin’s visual photograph. (b) illustrates the group with ideal spectra generated by an ideal array pattern (see Fig 4). (c) presents the group with more practical MVDR spectra generated by an  $8 \times 8$  patch antenna array.

much higher rendering speeds (exceeding 100 FPS). This method employs 3D Gaussian distributions (hereafter referred to as “Gaussians”) for geometry and spherical harmonics (SH) functions for radiance. Moreover, it introduces a rasterization pipeline that extensively accelerates both the training and rendering processes. Over the past year, substantial research has built upon 3DGS, exploring applications such as city-scale reconstruction [23], Structure-from-Motion (SfM) free 3D Gaussian Splatting [24], and 4D Gaussian Splatting with additional time domain [25].

### B. RF-3DGS

Returning to our context of radio propagation, the rays that render pixels of the image in the optical radiance field are equivalent to the MPCs that reach the Rx. Consequently, the pixel intensity corresponds to the MPC gain, and the image itself is equivalent to the radio AoA-gain spatial spectrum.

Inspired by such equivalence and the 3DGS method, we propose developing a similar approach for modeling radio wave propagation. However, radio waves differ significantly from visible light. Firstly, in wireless communication, we are concerned not only with the AoA-gain spectrum but also with other CSI, such as Angle of Departure (AoD) and delay of each path [26]. Secondly, due to the physical characteristics of radio waves, there is often a lack of detailed object geometric information in the ground truth radiance field, and limited spatial resolutions of radio devices.

In this paper, we propose RF-3DGS, a method that addresses the aforementioned challenges and enables rapid, precise, site-specific reconstruction of the Radio Frequency (RF) radiance field from very sparse training inputs. In addition to the inherited advantages of 3DGS, such as ultra-fast training and inference speeds, RF-3DGS distinguishes itself from visual

3DGS by not only reconstructing the last-bounce-only radiance field (AoA), but also encoding other CSI, such as Angle of Departure (AoD) and delay, into the SH functions, effectively addressing the first challenge. This enhanced radiance field representation allows for the efficient implementation of angle-domain management in massive Multiple Input Multiple Output (MIMO) systems, thereby avoiding the increasing computational complexity associated with pilot-based estimation as array size grows [27], [28]. Furthermore, this representation’s real-time inference and explicit geometry make it beneficial for other wireless system tasks, such as sensing and digital twin applications [29], [30], [31].

To address the second challenge, we explore various array signal processing techniques and propose a two-stage fusion training strategy that enables more precise geometry representation. Additionally, our method is specifically designed for massive MIMO systems, which demand the high-accuracy spatial spectra that RF-3DGS provides. These systems typically operate in the upper mid-band (7 to 16 GHz) or mmWave bands, where higher frequencies capture more geometric detail and enable larger array sizes, thereby offering significantly higher spatial resolution.

To demonstrate the performance of RF-3DGS, several test examples are presented in Fig. 1. Whether operating with the practical Minimum Variance Distortionless Response (MVDR) spectra generated by an  $8 \times 8$  patch antenna array or with ideal radio spatial spectra, which require more advanced and costly systems, RF-3DGS effectively reconstructs the radio radiance field in unvisited locations with very sparse input (only tens of samples in a complex environment). Moreover, RF-3DGS exhibits strong extrapolation capabilities thanks to the two-stage fusion training, which integrates visual geometric information into the representation. The effectiveness of RF-3DGS is evident in Fig. 1, where our method significantly

outperforms the State-of-The-Art (SOTA)  $NeRF^2$  [32].

Quantitatively, RF-3DGS achieves a substantially better Learned Perceptual Image Patch Similarity (LPIPS) [33] value in the reconstructed spatial spectra compared to  $NeRF^2$ , with an error reduction of 84.64%. LPIPS evaluates similarity between images by comparing deep features extracted from pretrained neural networks, providing a more robust measure of visual quality than other statistical metrics. Meanwhile, RF-3DGS requires only 3 minutes for RF radiance field reconstruction and just 2 ms to render a spectrum at an arbitrary array position, whereas  $NeRF^2$  takes 3 hours of training and approximately 1 second to render a new spectrum.

To further evaluate its effectiveness in wireless communication, the synthesized spatial spectra are utilized to generate Conventional Beamforming (CBF) steering vectors. The results indicate that in the ideal spectrum scenario, RF-3DGS accurately guides the steering angle with a median deviation of  $5.94^\circ$  at the test points. Moreover, since RF-3DGS also encodes additional CSI features, the AoD and delay channel spectra achieve LPIPS values of 0.395 and 0.382, respectively. We also assessed our digital twin framework by comparing it with physical twin measurements, which demonstrate a high degree of consistency with the physical reality.

### C. Contributions

Our contributions are summarized as follows:

- We utilize 3D reconstruction method from CV to wireless channel modeling, which can “render” 3D CSI at arbitrary locations in real-time (2 ms).
- We analyze differences between visible light and radio waves affect radiance field reconstruction, propose strategies to mitigate these effects, and explore various array signal processing techniques.
- We propose the RF-3DGS framework, which addresses two key challenges: 1) representing comprehensive CSI within a radiance field using CSI-encoded SH functions, and 2) fusing visual and radio data into the radiance field representation through a novel two-stage fusion training strategy. The whole pipeline only takes 3-minute in training.
- We construct a digital twin with a comprehensive radio spatial spectrum simulation pipeline and validate it using real-world measurements. Additionally, we demonstrate an ISAC scenario within this digital twin framework.

## II. PRIMER ON RADIO RADIANCE FIELD

In this section, we explore the rationale behind applying optical radiance field reconstruction methods to the RF domain. We will also highlight the critical factors that must be considered to ensure the successful adaptation of these methods.

### A. Visible Light and Radio Frequency: A Comparison

Although RF waves and visible light are both EM waves, their physical characteristics differ significantly. Firstly, in complex environments, the propagation behaviors of these two types of EM waves are markedly different, as illustrated in

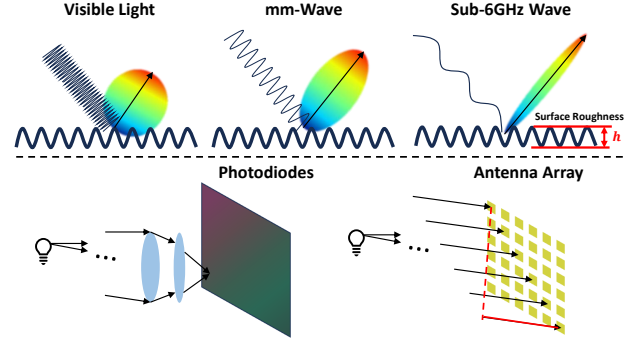


Fig. 2. RF and visible light wave comparison.

Fig. 2. For visible light, due to its short wavelength, most everyday surfaces do not meet the Rayleigh criterion for smoothness, which requires that the surface roughness height  $h$  be smaller than  $\lambda/(8 \cos \theta)$  (where  $\lambda$  is the wavelength and  $\theta$  is the incidence angle). Consequently, diffusion and scattering become the dominant interactions between visible light and surrounding objects, making these objects visible from almost all directions.

In contrast, for RF waves, especially those in the sub-6GHz range, specular reflection and diffraction are dominant [34], [35]. These interactions exhibit much higher directivity compared to scattering. While such interactions are favorable for wireless communication, providing signal coverage in Non-Line-of-Sight (NLoS) scenarios, they are less effective for “illuminating” objects. This means that the received radio waves contain less geometric information, which is crucial for the effectiveness of radiance field reconstruction methods.

Fortunately, as wireless communication frequencies extend into the mmWave range, surfaces tend to appear rougher, resulting in more scattering [36]. This enhances the opportunities to extract geometric information from received mmWave signals. Applications of mmWave imaging in surveillance and defense applications further demonstrate this characteristic [37], [38], [39], [40].

Secondly, the short wavelength of visible light allows the use of lenses to perfectly separate incoming rays based on their AoA to the millions of photodiodes in a handheld camera. For RF, constructing such an “optical” imager is physically challenging due to the limited number of effective elements within a constrained aperture. However, antenna arrays offer the advantage of capturing the response of each antenna element, including phase information, thereby enabling the use of array signal processing techniques to separate incoming RF signals and generate the radio spatial spectrum. This spectrum, representing signal strength at different AoAs, can be considered the “RF picture” captured by the antenna array. The quality of this picture, however, is still limited by the physical aperture size, the processing techniques, and the measurement devices.

### B. Radiance Field Reconstruction Methods

Radiance Field Reconstruction methods, including 3DGS, are based on volume rendering, which is typically used for

rendering transparent volumes such as fog and fire but can also be adapted to render solid objects due to its flexibility. Fig. 3 illustrates the basic concept of volume rendering. The rendering equation can be expressed as:

$$C = \int_{t_n}^{t_f} c(t, d) \cdot T(t) \cdot \alpha(t) dt, \quad (1)$$

$$T(t) = \exp \left( - \int_{t_n}^t \alpha(s) ds \right), \quad (2)$$

where  $C$  is the rendered pixel color,  $c(t, d)$  is the view dependent color at position  $t$ ,  $d$  is the view direction,  $\alpha(t)$  is the density, and  $T(t)$  is the transmittance, representing the integration of density from the image plane to  $t$ . When rendering a solid object, the ray intersects the object as shown in the figure, causing the transmittance  $T(t)$  to sharply drop from 1 to 0 due to the high density  $\alpha(t)$  at the object's surface. As a result, the portion of the ray behind the intersection has little contribution,  $Con(t) = \alpha(t)T(t)$ , to the pixel color. The free space portion before the intersection also contributes minimally due to the very small density  $\alpha(t)$ . This means that only the segment near the intersection significantly influences the pixel's color, which aligns with our visual experience.

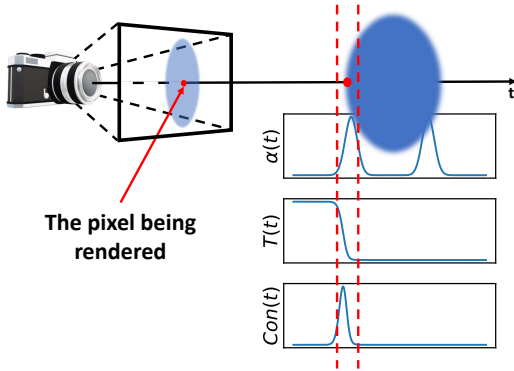


Fig. 3. Principles of volume rendering.

However, directly modeling and integrating such continuous fields  $c(t, d)$  and  $\alpha(t)$  is infeasible for most volumetric data. In [41], the integral function is discretized into multiple segments of length  $\delta_i$ , and the discrete volume rendering is formulated as:

$$C = \sum_{i=1}^N T_i (1 - \exp(-\alpha_i \delta_i)) c_i, \quad (3)$$

$$T_i = \exp \left( - \sum_{j=1}^{i-1} \alpha_j \delta_j \right). \quad (4)$$

To reconstruct the optical radiance field from images of the scene, we have a learnable representation capable of representing the radiance field and the geometry. This representation is subsequently optimized by iteratively rendering the rays corresponding to the images and performing gradient descent to minimize the loss between the rendered and ground truth colors. Furthermore, for more efficient training,

a well-designed representation structure, rendering pipeline, and training strategies are essential.

Beyond these techniques and representations, the fundamental philosophy behind how such methods capture scene geometry is straightforward: since a surface point on an object is visible from multiple views, the rays responsible for rendering this point converge from different camera positions to the same location. As a result, during gradient descent, only this surface point should receive an increase in density and an adjustment to its corresponding color, as this is the optimal solution to minimize the sum of the loss functions associated with those rays. This insight suggests that our radio spectra should also contain sufficient and accurate geometric information and maintain consistency across different views.

### C. Array Signal Processing and Spatial Spectrum

Considering applications in the wireless communication domain, we assume the system employs a common wireless communication configuration, typically involving half-wavelength spaced Uniform Planar Arrays (UPA) operating with either a digital beamformer or a fully analog beamformer to generate baseband digital signals. Systems specifically designed for RF imaging/radar are not considered in this paper.

In a typical array signal processing scenario [42], there are  $M$  signals incident from different directions onto the array, received by the  $N$  elements of the UPA, and processed by the  $L$  steering vectors, resulting in the desired signal intensities  $\mathbf{y}(t)$  across the  $L$  scanning directions. This process can be expressed as:

$$\mathbf{y}(t) = \mathbf{W}^H \cdot \mathbf{A}(\Theta, \Phi) \cdot \mathbf{s}(t) + \mathbf{n}(t). \quad (5)$$

The signal vector  $\mathbf{s}(t)$  is defined as:

$$\mathbf{s}(t) = [s_1(t), s_2(t), \dots, s_M(t)]^T, \quad (6)$$

where  $s_m(t)$  represents the  $m$ -th incident signal characterized by its incident zenith angle  $\theta_m$  and azimuth angle  $\phi_m$ .  $\mathbf{n}(t)$  is the additive white Gaussian noise.

The matrix  $\mathbf{A}(\Theta, \Phi)$  is a complex matrix of size  $N \times M$ , with each column corresponding to the array manifold vector of the  $m$ -th signal:

$$\mathbf{A}(\Theta, \Phi) = [\mathbf{a}(\theta_1, \phi_1), \mathbf{a}(\theta_2, \phi_2), \dots, \mathbf{a}(\theta_M, \phi_M)], \quad (7)$$

where each array manifold vector  $\mathbf{a}(\theta, \phi)$  is the product of the antenna pattern gain  $G(\theta, \phi)$  and the phase differences caused by the path differences  $\mathbf{d}(\theta, \phi)$  between each element and a reference location:

$$\mathbf{a}(\theta, \phi) = G(\theta, \phi) \cdot e^{-j \frac{2\pi \mathbf{d}(\theta, \phi)}{\lambda}}. \quad (8)$$

Thus, the element responses are:

$$\mathbf{x}(t) = \mathbf{A}(\Theta, \Phi) \cdot \mathbf{s}(t). \quad (9)$$

The objective in our case is to find an appropriate steering vector set  $\mathbf{W}^H = [w_1, w_2, \dots, w_L]$ , that maximize the Signal-to-Interference-plus-Noise Ratio (SINR) of the signals in each corresponding AoA direction.

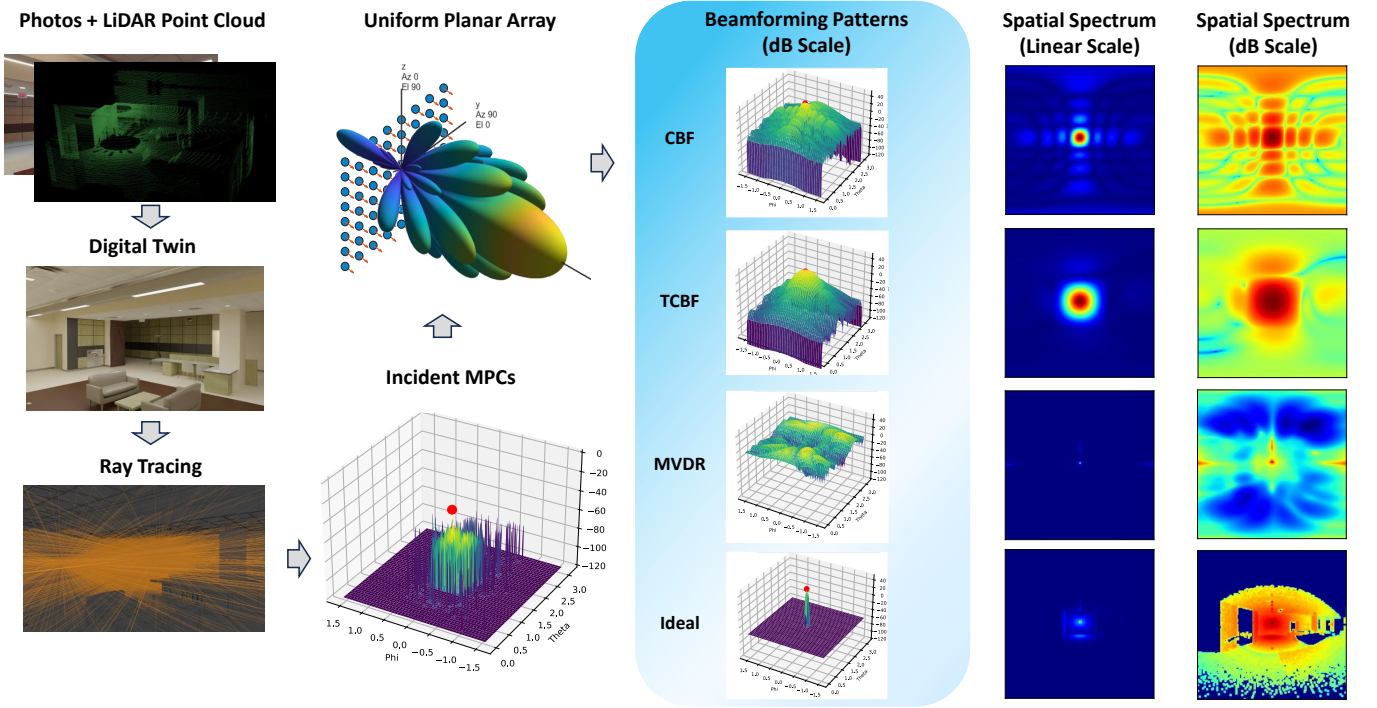


Fig. 4. Full radio simulation pipeline with various beamforming patterns and their corresponding spectra.

In our context of massive MIMO systems operating at mmwave bands within a fully scattering environment, we can obtain the estimated signal intensities  $s(t)$  across a set of scanning directions and then be organized into the desired spatial spectrum. However, directly using intensity as the pixel value introduces a notable issue. For EM wave propagation in free space, the pathloss follows the well-known Friis equation:

$$P_r = P_t \frac{G_t G_r \lambda^2}{(4\pi d)^2}, \quad (10)$$

where  $d$  is the distance between the Tx and Rx. This equation indicates that the received power decreases proportionally to  $1/d^2$ . Referring back to Fig. 3 and Eqn. 1, we note that along a ray, the rendered color is entirely independent of the distance between the object surface and the camera. This is consistent with our experience; for example, when viewing an LED bulb from 1 m and then 2 m away, the perceived brightness does not drop by four times.

This discrepancy between the Friis equation and volume rendering can be explained by the human eye's response to light intensity, which follows a logarithmic-like curve and spans a dynamic range of approximately 100 dB [43]. Therefore, to adapt NeRF-style methods to our context, the spectrum must undergo a similar transformation. In this paper, we convert the AoA-gain spectrum to the dB scale to mimic such distance-independent decay.

#### D. Spatial Spectrum

To accommodate different wireless systems, we explored various array signal processing techniques to provide an overview of spectra that different systems can generate, as

shown in Fig. 4. The impact of these spectra on radio radiance field reconstruction will be further illustrated in the next section.

**CBF**, also known as the Bartlett beamformer [44], is a delay-and-sum beamforming technique. It adjusts the phase shifts of each array element to align their wavefronts in the desired scanning direction  $(\theta_l, \phi_l)$ . The CBF steering vector only compensates for phase differences, expressed as:

$$\mathbf{w}_{\text{CBF}}(\theta_l, \phi_l) = \frac{\mathbf{a}(\theta_l, \phi_l)}{\|\mathbf{a}(\theta_l, \phi_l)\|}. \quad (11)$$

Therefore, CBF requires only an analog beamforming system with phase shifters and a single RF chain. Fig. 4 illustrates the CBF pattern, which acts as a kernel convolved with incoming MPCs to form the spatial spectrum. This kernel exhibits numerous strong side lobes, leading to significant interference in the spectrum, even when represented on a linear scale. Furthermore, this kernel varies with different steering angles, complicating frequency-domain deconvolution for interference reduction [45].

To address this issue, we tested the CBF spectrum tapered by a Hann window [42] and found that while side lobe levels were suppressed, interference remained problematic on the dB scale. Consequently, we adopted the *NeRF<sup>2</sup>* configuration, using a linear scale transform and per-view normalization for both CBF and Tapered CBF (TCBF) spectra. While this configuration effectively represents AoA in small environments, it contradicts the distance-independent decay and view consistency assumptions of NeRF-style methods, resulting in poor performance in larger environments.

**MVDR**, also known as the Capon beamformer [46], is a popular array signal processing technique characterized by its adaptive ability to maximize the SINR. Unlike CBF, which merely maximizes gain in the current scanning direction, MVDR optimizes the steering vector  $\mathbf{w}$  by solving the following problem:

$$\min_{\mathbf{w}} \mathbf{w}^H \mathbf{R} \mathbf{w} \quad \text{subject to} \quad \mathbf{w}^H \mathbf{a}(\theta_l, \phi_l) = 1, \quad (12)$$

where  $\mathbf{R} = \mathbf{x}(t)\mathbf{x}^H(t)$  is the signal autocorrelation matrix. The optimal steering vector and the corresponding power spectrum can be written as:

$$\mathbf{w}_{\text{opt}} = \frac{\mathbf{R}^{-1} \mathbf{a}(\theta_l, \phi_l)}{\mathbf{a}^H(\theta_l, \phi_l) \mathbf{R}^{-1} \mathbf{a}(\theta_l, \phi_l)}, \quad (13)$$

$$P_{\text{MVDR}}(C) = \frac{1}{\mathbf{a}^H(\theta_l, \phi_l) \mathbf{R}^{-1} \mathbf{a}(\theta_l, \phi_l)}. \quad (14)$$

As shown in Fig. 4, the MVDR spectrum in both linear and dB scales has much higher resolution and significantly reduced interference, revealing some geometric structure of the scene. However, MVDR has two key limitations: it requires individual element responses, needing a full digital beamforming system, and it is sensitive to signal distortion due to its reliance on the autocorrelation matrix  $\mathbf{R}$ .

**Space Alternating Generalized Expectation maximization (SAGE)** algorithm [47] is an iterative technique for parameter estimation, particularly effective in array signal processing [48], [49], [50], [51]. However, its computational complexity escalates with the number of MPCs, making it less suitable for generating a complete spatial spectrum. Consequently, in our study, SAGE was only employed for extracting MPCs from field measurements.

### E. Conclusion

Based on the above discussion, the following requirements for radio spectra are essential for the success of radiance field reconstruction methods:

- The spectra should convey maximal geometric information.
- The objects within the spectra should remain consistent across different views.
- The spectral intensity should follow transformations that minimize the impact of distance-dependent decay.

## III. RELATED WORKS

**Traditional Methods:** Radio propagation modeling has been extensively studied over the decades. Empirical models, such as the Okumura-Hata [2] and COST 231 models [3], are widely used for predicting approximate path loss in large-scale environments. Computational EM simulations [6], utilizing acceleration methods like the finite-difference time-domain (FDTD) method [7], offer high accuracy for applications such as antenna design [8] or near-field simulations [9]. While these methods are effective for specific tasks, they fall short in more general scenarios.

**Ray tracing:** Originally developed for computer graphics, ray tracing has long been adapted for radio propagation modeling [52], [53]. It models radio waves as rays to simulate

complex RF interactions such as reflection, diffraction, and scattering [10], [11], [12], [13], [14]. Although ray tracing is suitable for a wide range of environments, it is limited by high computational complexity, stringent requirements for environmental information, and an inflexible pipeline that is difficult to calibrate.

**Neural Network Methods:** These methods use broader environmental information as input to generate outputs such as CSI [54], [55] or 2D path loss maps [56], [57]. Although these approaches are fast, provide acceptable accuracy, and perform well within the domain defined by the training data, they lack determinism and interpretability.

**Radiance Field Reconstruction Methods:** Since the success of radiance field reconstruction methods in CV, several works have extended these methods to the RF domain. We briefly introduce some of them here.

*NeRF<sup>2</sup>* reconstructs a “squared” radio radiance field that considers both “camera” and “light source” locations as inputs. However, its spectra, generated using CBF at 915 MHz with linear scale transformation and per-view normalization, suffer from strong interference, inconsistencies across views, lack of geometric information, and distance-dependent decay, all of which conflict with the requirements discussed earlier. To maintain effectiveness, *NeRF<sup>2</sup>* requires a sample density  $2000\times$  higher than in this work, negating the advantage of sparse sampling that NeRF offers. RayProNet [58] integrates environmental information as input and uses an explicit “light probe” as the radio radiance field voxel. However, RayProNet is limited to producing only 2D path loss maps, without offering more detailed information.

## IV. PROPOSED RF-3DGS FRAMEWORK

As previously mentioned, although 3DGS has set a new benchmark in optical radiance field reconstruction, two critical challenges must be addressed to adapt it for the RF domain. The first challenge arises from the differences between typical novel view synthesis tasks and wireless communication. In most optical radiance field reconstruction scenarios, scenes are assumed to have static lighting with arbitrary camera poses, and the only point of interest is the photograph. Consequently, the last-bounce-only volume rendering method is well-suited to this context, as it records how the static radiance arrives at the camera from the last interacted object, disregarding prior propagation.

In wireless communication, the situation is more complex. Typically, we also assume a fixed Tx and a moving Rx, with the “picture” being the AoA-gain spatial spectrum. Although this spectrum is valuable, massive MIMO systems often require more detailed CSI on the Tx side, where the larger size array is typically used to achieve more precise beamforming and serve multiple Rxs. Additionally, other CSI features such as delay, phase, and polarization are also vital for wireless communication systems. In RF-3DGS, we address this challenge by developing CSI-encoded SH functions to represent these essential path characteristics.

The second challenge is the difficulty of obtaining sufficient geometric information from the radio spatial spectrum,

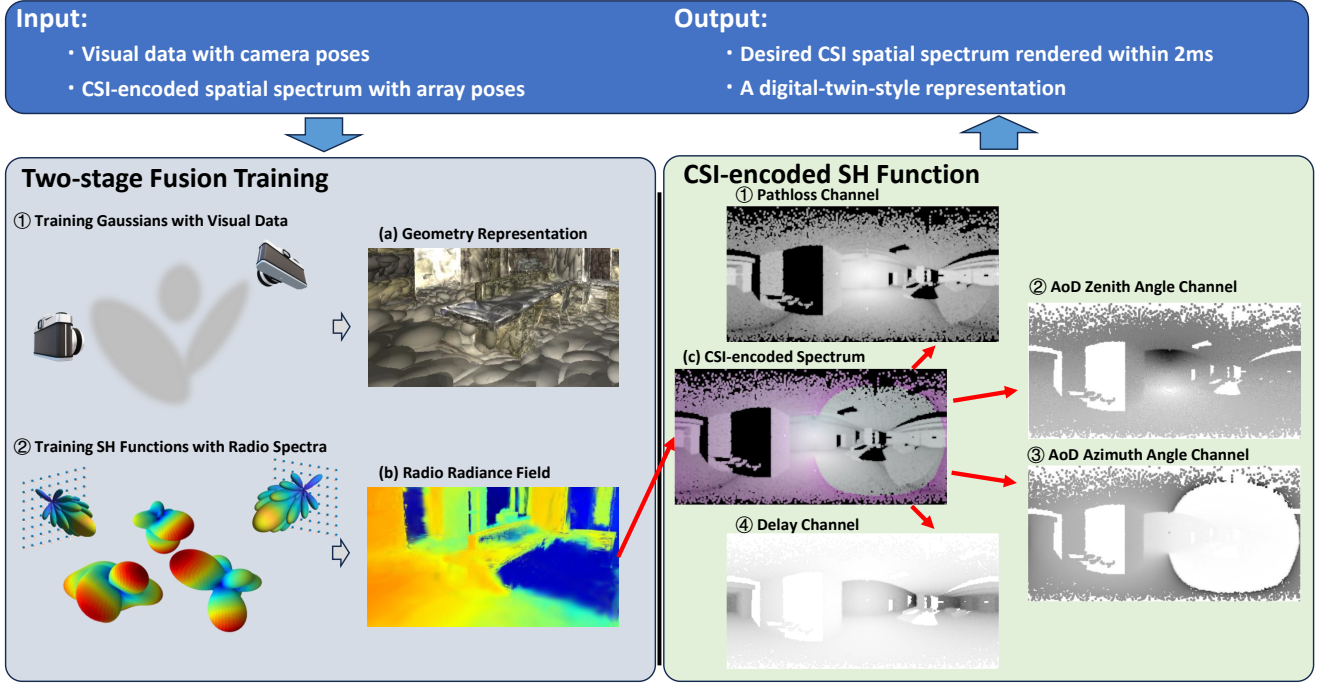


Fig. 5. RF-3DGS pipeline. (a) The extracted geometry representation from the visual data, consisting of millions of Gaussians, where the Gaussians are visualized by their contour surfaces. (b) The reconstructed radio radiance field, where the objects are illuminated by RF waves. (c) An example of the CSI-encoded spectrum and the corresponding decoded CSI spectra from the respective channels.

as discussed in Sec. II. Although massive MIMO systems operating in mmWave bands mitigate this issue to some extent, finding an appropriate method to accurately capture scene geometry remains critical. To address this, RF-3DGS proposes a two-stage fusion training strategy that integrates visual data and RF data for enhanced training, along with multiple array processing techniques, thereby ensuring the effectiveness of radiance field reconstruction.

#### A. RF-3DGS Overview

Building upon the foundations of 3DGS, RF-3DGS adopts a similar representation structure and rasterization rendering pipeline. As illustrated in Fig. 5, RF-3DGS uses visual images and radio spatial spectra as training targets, with the corresponding camera/array poses as input to render the predicted spectra, applying gradient descent to refine the representations.

For geometry representation, RF-3DGS utilizes 3D Gaussian distributions, each with learnable parameters, including density values  $\alpha$ , positions (mean  $(x, y, z)$ ), and shapes. The shape can be loosely visualized as an “ellipsoid” controlled by a quaternion  $\mathbf{q}$  for rotation and a 3D scaling vector  $\mathbf{s} \in \mathbb{R}^3$ , equivalent to the  $3 \times 3$  covariance matrix of the 3D Gaussian. During the adaptive training process, these quantities—density, positions, and shapes—are optimized to accurately represent the ground truth scene geometry. For view-dependent radiance representation, RF-3DGS assigns CSI-encoded SH functions to each Gaussian, encapsulating the CSI of paths departing from the Gaussian in all directions.

These representations define a field equation that can be directly integrated without relying on complex and lossy

sampling strategies. Instead of integrating the rays one by one, RF-3DGS, inheriting from 3DGS, utilizes an efficient rasterization rendering pipeline, which is well-suited to GPU computational structures. This rasterization process can be interpreted as splatting the “ellipsoids” onto the image plane, forming overlapping 2D ellipses that constitute the final image. Consequently, the loss function is defined as the L1 loss plus a differential Structural Similarity Index Measure (SSIM) loss term between the target image and the rendered image. The gradient descent then backpropagates from this loss through the differentiable rasterization pipeline to the learnable parameters of each Gaussian that is visible from the current camera perspective. Further details on how this pipeline handles view splitting, GPU memory management, and rasterization acceleration can be found in [22].

Despite the specifics of the rasterization process, the rendering process for each ray remains equivalent to the continuous volume rendering formula, as shown in Eqn. (1). This implies that the requirements for the spectra remain consistent with those proposed in Sec. II-E.

#### B. CSI-encoded SH Function

To begin, it is essential to understand how SH functions work. This approach employs a linear combination of simple orthogonal basis SH functions to represent a complex spherical function. The number of basis functions is determined by the degree; the higher the degree, the more basis functions are available, allowing for the representation of more complex functions. This means SH functions are most effective if the represented spherical function exhibits continuity in the angle

domain. When this continuity is absent, a significantly higher degree of SH functions is required, leading to impractical complexity.

Returning to our discussion, while the last-bounce-only volume rendering may initially seem disconnected from the representation of other CSI features, such as delay and AoD, a more detailed analysis reveals a significant correlation between these features and the path geometry when examined across different paths.

Consider, for instance, a cluster of MPCs reflected from a desk into a fixed Rx array. These MPCs exhibit not only continuous channel gains, as shown in the AoA-gain spectrum (Fig. 1), but also continuous delay and AoD values due to their closely located paths. This correlation extends to MPCs originating from the same Gaussian and arriving at nearby camera positions. The generated CSI spectra (Fig. 5) validate this assumption. These two types of continuity—continuity from one Gaussian to adjacent camera positions and from different AoAs to one camera position—suggest that they can be effectively represented using the SH functions assigned to each distinct Gaussian.

Thus, along with the AoA-gain spectrum, the other CSI features can be encoded using parallel channels, much like how visual images encode RGB values. In this study, we focus on encoding AoD and delay, both of which are critical in wireless communication and sensing. Specifically, for AoD, we decompose it into two channels: one encoding the azimuth angle ( $0-360^\circ$ ) and the other encoding the zenith angle ( $0-180^\circ$ ). Given that the significance of each path is primarily determined by its channel gain, the AoD values are scaled by a gain coefficient, which equals the normalized channel gain within the range of  $(0,1)$ . The subsequent experimental results demonstrate that RF-3DGS can effectively capture CSI spectra and accurately predict such spectra at test locations.

### C. Two-stage Fusion Training

From Fig. 4, even the ideal spectrum can only be considered as low-quality “photos” with other spectra offering even less geometric information. Thus, in RF-3DGS, we assume access to both the radio spatial spectra and visual data, which serves as a low-cost supplement to geometric information. The proposed two-stage fusion training process is designed to extract geometric information from the visual data to enhance the radio radiance field representation.

Before beginning the training, if the visual data consists of photos or video without camera intrinsic and extrinsic parameters, an initialization process is required to estimate these parameters and generate initial point clouds using SfM. Otherwise, this process can be skipped, allowing training to start from random point clouds.

Once initialization is complete, the first stage of training begins with a warm-up phase. During this phase, the Gaussians are trained using resolution-reduced images, enabling them to quickly capture global geometry rather than getting stuck on optimizing fine details. The image resolution is doubled twice, after 250 and 500 iterations, until the original resolution is reached.

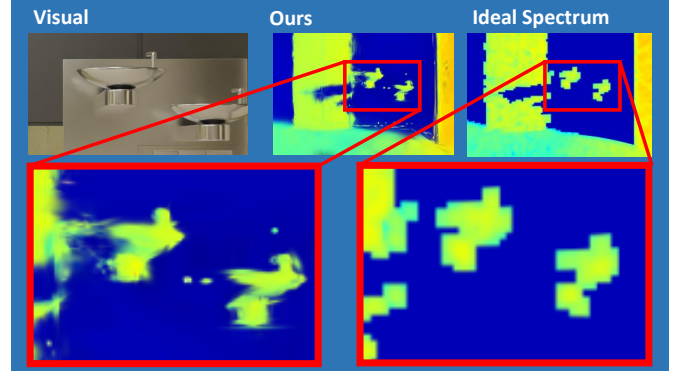


Fig. 6. Extrapolation ability of the proposed two-stage fusion training. Both spectra are rendered using the same  $300 \times 200$  pinhole camera model. The ideal spectrum, serving as the training target, is limited by the maximum MPCs our RTX A6000 48GB GPU can handle and the minimum array pattern lobe width needed for spectrum continuity.

Following the warm-up, a periodic densification process refines the Gaussians every 100 iterations. In regions where the number of Gaussians is insufficient to represent intricate 3D geometry, the densification process splits large Gaussians and clones small Gaussians to create more learnable “ellipsoids” in those regions. Gaussians with very small density values or those with excessively large footprints in the views are removed to prevent the “floater” problem, a common issue in radiance field reconstruction methods.

To manage the quantity of Gaussians, their  $\alpha$  values are reset towards zero every 3,000 iterations. This reset allows key Gaussians to quickly regain their original density values during optimization, while abnormal or unnecessary Gaussians, whose density values increase slowly, are removed in subsequent densification steps.

After establishing a well-trained geometry representation, the second stage begins. In this stage, RF-3DGS uses the collected radio spectra to train the CSI-encoded SH functions and the density of each Gaussian, while freezing the positions  $(x, y, z)$ , rotation  $\mathbf{q}$ , and scaling  $\mathbf{s}$ . After optimization, the new CSI-encoded SH functions can be interpreted as the objects being re-illuminated by a fixed Tx radio, with the RGB color channels corresponding to different CSI features.

The advantage of the proposed two-stage fusion training is not only that it requires low-cost visual data as a supplement, but also exhibits extrapolation capabilities, as shown in Fig. 6. This capability arises from the accurate visual geometric information, which provides the actual radiance source location, allowing vague or interfered radio spectra to be mapped to the correct locations rather than being assigned to vague floaters, as seen in *NeRF*<sup>2</sup>.

## V. DATASET, RESULT, AND PERFORMANCE EVALUATION

**Dataset:** In this paper, we constructed a digital twin framework to evaluate the effectiveness of RF-3DGS, comprising comprehensive field measurements in a  $14 \times 15$  m<sup>2</sup> lobby and a digital replica of the same space with a full radio simulation pipeline. The 60 GHz measurement data [59] was provided by the National Institute of Standards and Technology (NIST),

USA. For the performance experiments presented in this section, we mainly utilize the simulation-based dataset. The simulator used is Sionna [60], an open-source communication simulator developed by NVIDIA, which is equipped with the Sionna RT [61] ray tracer and supports GPU acceleration.

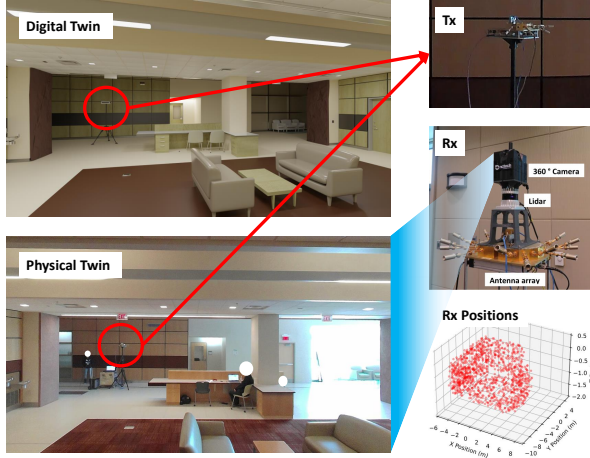


Fig. 7. Dataset overview. Our dataset consists of field measurements provided by NIST [59], along with a simulated digital replica conducted under the same configuration and environmental conditions.

As shown in Fig. 7, our simulation playground is an accurate 3D replicated model of the NIST lobby with a fixed Tx, and the radio spectra are captured from a set of sparse random Rx positions distributed throughout the lobby. Since the setup is designed to simulate a fully diffuse environment at 60 GHz, the number of paths between each Tx-Rx pair often exceeds 300,000, requiring the array size to be limited to around  $10 \times 10$ . More details on the simulation configuration and settings can be found in our open-source code.

**Performance of Radiance Field Reconstruction:** In this part, we focus on evaluating the radiance field reconstruction performance. The dataset, consisting of 800 samples, splits into fixed 160 test samples and 640 training samples. Furthermore, the training samples were randomly selected in proportions of 20%, 40%, 60%, 80%, and 100%.

We compared our method, RF-3DGS, with the Conditional GAN (CGAN) [62], representing black-box neural network approaches, and the SOTA  $NeRF^2$ . The results are presented in Fig. 8.

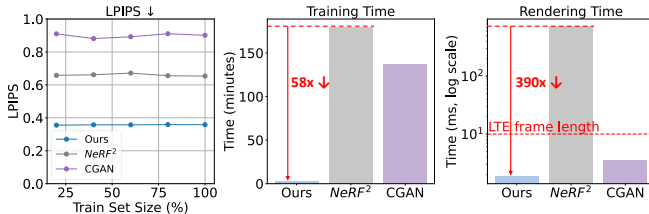


Fig. 8. General comparison.

In general, RF-3DGS demonstrates significantly better LPIPS scores, requires significantly shorter training times, and offers rendering speeds faster than LTE frame rates.

Additionally, RF-3DGS achieves high reconstruction quality with very sparse training samples, with rendering quality substantially degrading only when the sample count drops below approximately 20, depending on the uniformity of the sample distribution. For evaluating other parameters, we utilized the full training set to analyze their impact.

In contrast,  $NeRF^2$  struggles to capture detailed scene information, resulting in degraded LPIPS performance. As illustrated in Fig. 9,  $NeRF^2$  can only reconstruct large, illuminated floaters with limited details. Moreover, its training process takes approximately 3 hours, with each rendering requiring around one second.

For CGAN, the generator synthesizes images while the discriminator evaluates their fidelity, guiding the generator’s optimization. The challenge lies in our sparse training input, where test inputs differ significantly from the training data. Consequently, the generator struggles to learn the mapping between Rx poses and target images, and the discriminator fails to provide useful gradients, resulting in poor overall performance.

**Insufficiency of Statistical Metrics:** Another crucial point is that only high-level metrics, such as LPIPS (lower is better), can effectively evaluate our spectra. Traditional statistical metrics, such as the Peak Signal-to-Noise Ratio (PSNR) and SSIM, fall short. This issue has been widely discussed in the CV domain [33], [63]. As illustrated in Fig. 9, even though the spectrum predicted by our method is visibly of higher quality, the PSNR and SSIM yield similar values for both spectra, while only LPIPS reflects the difference accurately.

The primary reason for this metric failure is that our scenario differs significantly from other visual task comparisons. In typical visual tasks, like evaluating compression or super-resolution, outputs are usually close to the perfect ground truth images, resulting in high metric scores (PSNR > 35 dB, SSIM > 0.9, LPIPS < 0.05), where errors are mostly pixel-wise.

In contrast, in our tasks, the reconstruction performance is considerably worse, with PSNR around 15 dB, SSIM around 0.5, and LPIPS around 0.4, and the ground truth also contains distortions and noise. These factors reduce the metric discriminative power, as critical errors, such as the loss of geometric structure, are obscured by less significant noisy errors. This issue is particularly severe for PSNR and SSIM, which heavily rely on statistical features, unlike LPIPS, which utilizes convolutional neural networks to extract “deep” features for similarity evaluation.

**Impacts of Different Spectra:** To further evaluate the effects of different types of spectra, we trained RF-3DGS using CBF, TCBF, and MVDR spectra, testing them against both their corresponding homogeneous ground truth and the ideal spectrum ground truth. These two tests serve distinct purposes: first, homogeneous spectrum testing evaluates how spectra interference and inconsistency impact RF-3DGS’s reconstruction ability; second, ground truth testing assesses how these spectra degrade reconstruction quality. Fig. 9 provides a detailed comparison.

From the comparison, it is clear that the CBF and TCBF spectra impair both reconstruction ability and quality, evident from their poor performance across all metrics. The degrada-

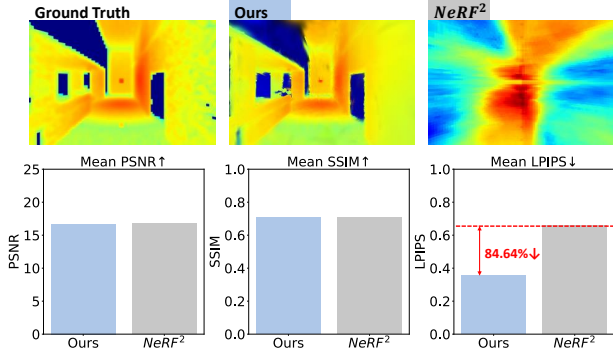


Fig. 9. Limitation of Statistical Metrics. Statistical metrics are significantly affected by noisy errors, making them insufficient for capturing and emphasizing critical errors such as the loss of geometric structure in the  $NeRF^2$  spectra. High-level metrics, such as LPIPS, are more appropriate for evaluating similarity in our task.

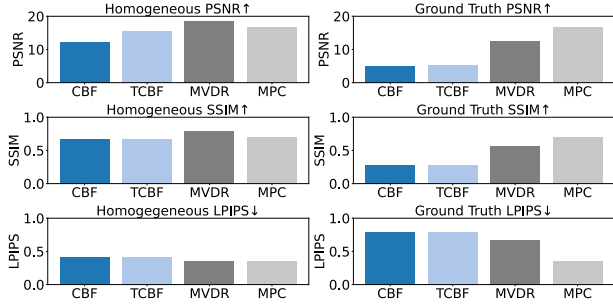


Fig. 10. Impacts of different spectra.

tion in reconstruction quality is even more pronounced, with PSNR dropping to 5 dB. This suggests that for CBF and TCBF spectra, strong interference, lack of geometric information, and distance-dependent decay severely limit the effectiveness of radiance field reconstruction in large environments.

In contrast, the MVDR spectrum group exhibits much higher performance in both testing scenarios. More interestingly, in homogeneous spectrum testing, the MVDR spectrum group even results in higher PSNR and SSIM compared to the ideal spectrum group, which may appear counter-intuitive given the ideal spectrum's higher quality and lower interference. However, as shown in Fig. 6, our method has an extrapolation ability that provides more details than the ideal spectrum. This extrapolation results in lower performance in statistical metrics like PSNR and SSIM but yields similar evaluations from LPIPS, further validating the effectiveness of the LPIPS metric in our tasks.

In summary, these comparisons demonstrate that RF-3DGS achieves significantly higher radio radiance field reconstruction quality, faster training and rendering speed compared to other methods. Additionally, RF-3DGS requires only tens of samples to reconstruct the radiance field across a large lobby while providing an explicit geometric representation. These features and high performance underscore the potential of RF-3DGS in upcoming 6G network applications.

**Application in Wireless Communication:** To evaluate the effectiveness of RF-3DGS in wireless communication, we

consider an application scenario where the Rx-side AoA-gain spectra are used to guide the Rx array in performing angle-domain CBF for signal reception. In this context, the AoA of the maximum-gain path is primary concern. The following results illustrate the angle deviation of RF-3DGS with different types of spectra. As shown, although the CBF and TCBF spectra fail to accurately represent the scene geometry, they can still support simple beamforming tasks, though with some performance loss.

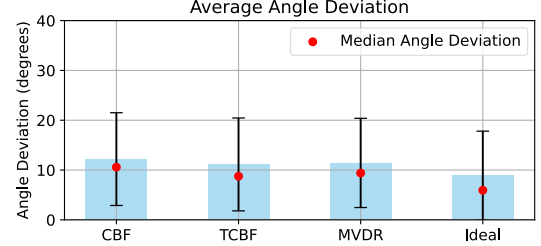


Fig. 11. Angle deviation of CBF guided by spectra.

**CSI-spectrum Prediction:** Another key feature of RF-3DGS is its capability to encode comprehensive CSI. In this paper, we tested its capability to represent the AoD and delay, which are critical in wireless communication.

As shown in Fig. 12, the results indicate the ability of RF-3DGS to reconstruct Rx-side AoA-AoD spectra and AoA-delay spectra. We also present examples of the decoded CSI spectra in Fig. 5. For the delay channel, we use normalized delay values, measured from the first arrival of MPCs, which is more practical and helps mitigate distance-dependent decay. The example demonstrates that the delay increases from the near reflection point to the far end, similar to a depth image. In the AoD-azimuth channel, although the angles vary according to physical laws, a sharp edge corresponding to the transition between 0 and  $360^\circ$  is visible. A more appropriate approach would involve using a 3D unit vector to represent such AoD information; however, in this paper, we use these two angles for a more intuitive demonstration.

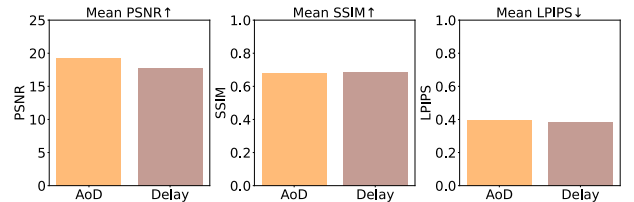


Fig. 12. Accuracy of encoded CSI spectra.

## VI. FIELD STUDY: A DIGITAL RADIO TWIN

In previous experiments, our testing relied on simulation datasets, raising concerns about potential discrepancies between our digital twin and its physical counterpart. In this section, we demonstrate the fidelity of our digital radio twin framework, which includes both environment geometry and a comprehensive radio radiance field, and highlight its support for advanced applications like ISAC.

**Calibrating Radiance Field:** To validate the fidelity of our generated spectra, we first overlay them with equirectangular photographs taken from the same positions. The results show that most spectra align well with the visual geometry, as illustrated in Fig. 13.

We also conducted field measurements at the same Rx locations using a synchronized Tx-Rx system, as depicted in Fig. 7. This system generates high-definition, precise Channel Impulse Response (CIR) between each Tx and Rx array element pair, which are processed by the SAGE algorithm to estimate key MPCs, including path loss, delay, AoD, and AoA. More details about this system are available in [51], [59]. Using these MPCs, we generated an MPC spectrum similar to our ideal spectra, which was then used to validate and calibrate our digital twin. The lower image of Fig. 13 shows the comparison results of direct validation and after calibration.

Two limitations in the field measurement process affect direct validation performance: the limited Rx vertical FoV, indicated by the red lines in Fig. 13 which also applies to Tx, and the system’s reliance on SAGE algorithms, which only estimate dominant MPCs. Consequently, the spectrum contains little information beyond several discrete MPCs.

This scenario is common when real systems have imperfections. In these cases, the advantages of RF-3DGS, such as rapid training and extrapolation ability, become particularly valuable. With just 3 minutes of re-training, we can produce a validated radio radiance field representation with high testing metrics, as shown in Fig. 14. The extrapolation capability also allows us to map imperfect measurements onto the correct positions.

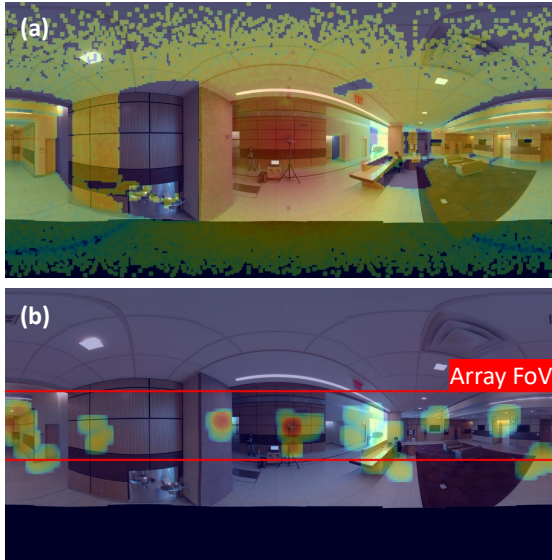


Fig. 13. Comparison of (a) digital twin and (b) physical twin measurements [59].

**An ISAC Scenario Demo:** Considering RF-3DGS’s remarkable ability to reconstruct the radio radiance field and model the environment with real-time wireless communication feedback, its potential in ISAC applications [29] becomes evident. Fig. 15 illustrates an ISAC scenario. On the left,

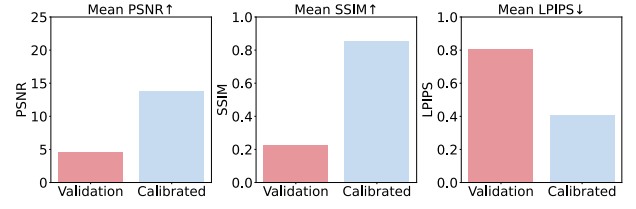


Fig. 14. Calibration with field measurement.

the spectra rendered using the well-trained RF-3DGS representation serve as prior knowledge. Then, a person enters the scene. Traditional methods might struggle to capture and render such dynamic changes in real-time [64], [65]. However, with RF-3DGS, the system not only detects the individual’s presence but also quickly generates a highly detailed radio spatial spectrum from the communication feedback, accurately reflecting the person’s shape and location within the scene by comparing the captured spectra with those rendered from the prior representation

This capability is particularly beneficial in environments where timely and accurate sensing is crucial, such as in safety monitoring or automated navigation systems. RF-3DGS enables the simultaneous acquisition of communication signals and precise reconstruction of the surrounding environment’s geometry in an explicit manner.

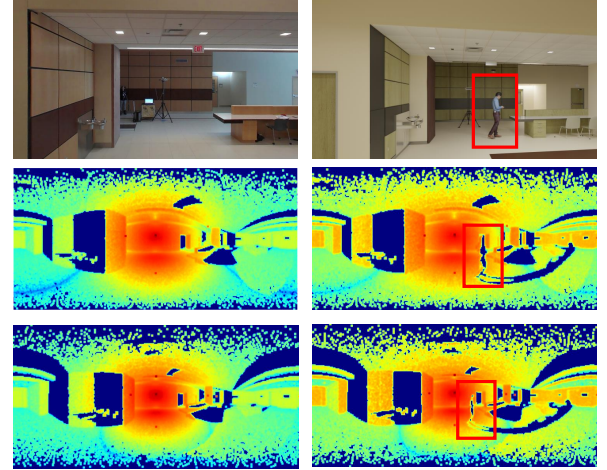


Fig. 15. ISAC scenario demonstration. The left figures depict the well-trained radio radiance field representation, which serves as prior knowledge. The right figures illustrate the real-time scenario, where the wireless channel feedback is compared to the prior to locate the sensing target.

## VII. CONCLUSIONS

In this paper, we proposed RF-3DGS, a fast and efficient radio radiance field reconstruction method that demonstrates high performance in reconstruction quality. RF-3DGS significantly reduces the training time to just a few minutes, requires only 2 ms to render a spectrum, and needs only tens of samples to reconstruct a scene while providing an explicit geometry representation. We also showcased several applications of RF-3DGS and introduced a digital twin framework to validate and enhance the reconstruction process.

However, several challenges persist. A primary issue is the difficulty in obtaining accurate CSI spatial spectra. Addressing

this challenge may necessitate the design of specialized equipment or the adaptation of techniques from mmWave imaging and radar systems for radio radiance field reconstruction. Additionally, the inconsistency between visual geometry and RF geometry, where certain materials appear very different or even transparent in RF, presents another potential challenge. Furthermore, exploring more practical applications to fully leverage the benefits of RF-3DGS in 6G networks, particularly in areas such as cell-free massive MIMO and ISAC, remains a crucial avenue for future research.

## REFERENCES

- [1] D. Tse, "Fundamentals of wireless communication," *Cambridge University Press google scholar*, vol. 2, pp. 281–302, 2005.
- [2] A. Medeis and A. Kajackas, "On the use of the universal okumura-hata propagation prediction model in rural areas," in *VTC2000-Spring. 2000 IEEE 51st Vehicular Technology Conference Proceedings (Cat. No. 00CH37026)*, vol. 3, pp. 1815–1818, IEEE, 2000.
- [3] Y. Singh, "Comparison of okumura, hata and cost-231 models on the basis of path loss and signal strength," *International journal of computer applications*, vol. 59, no. 11, 2012.
- [4] P. Series, "Propagation data and prediction methods for the planning of indoor radiocommunication systems and radio local area networks in the frequency range 900 mhz to 100 ghz," *Recommendation ITU-R*, pp. 1238–7, 2012.
- [5] V. Erceg, L. J. Greenstein, S. Y. Tjandra, S. R. Parkoff, A. Gupta, B. Kulic, A. A. Julius, and R. Bianchi, "An empirically based path loss model for wireless channels in suburban environments," *IEEE Journal on selected areas in communications*, vol. 17, no. 7, pp. 1205–1211, 1999.
- [6] A. Bondeson, T. Rylander, and P. Ingelström, *Computational electromagnetics*. Springer, 2012.
- [7] D. M. Sullivan, *Electromagnetic simulation using the FDTD method*. John Wiley & Sons, 2013.
- [8] A. Hoofar and V. Jamnejad, "Electromagnetic modeling and analysis of wireless communication antennas," *IEEE microwave magazine*, vol. 4, no. 1, pp. 51–67, 2003.
- [9] A. Yaghjian, "Efficient computation of antenna coupling and fields within the near-field region," *IEEE Transactions on antennas and Propagation*, vol. 30, no. 1, pp. 113–128, 1982.
- [10] Z. Yun and M. F. Iskander, "Ray tracing for radio propagation modeling: Principles and applications," *IEEE access*, vol. 3, pp. 1089–1100, 2015.
- [11] R. Charbonnier, C. Lai, T. Tenoux, D. Caudill, G. Gougeon, J. Senic, C. Gentile, Y. Corre, J. Chuang, and N. Golmie, "Calibration of ray-tracing with diffuse scattering against 28-ghz directional urban channel measurements," *IEEE Transactions on Vehicular Technology*, vol. 69, no. 12, pp. 14264–14276, 2020.
- [12] T. Orekondy, P. Kumar, S. Kadambi, H. Ye, J. Soriaga, and A. Behboodi, "Winert: Towards neural ray tracing for wireless channel modelling and differentiable simulations," in *The Eleventh International Conference on Learning Representations*, 2022.
- [13] F. Hossain, T. K. Geok, T. A. Rahman, M. N. Hindia, K. Dimiyati, S. Ahmed, C. P. Tso, and N. Z. Abd Rahman, "An efficient 3-d ray tracing method: Prediction of indoor radio propagation at 28 ghz in 5g network," *Electronics*, vol. 8, no. 3, p. 286, 2019.
- [14] U. R. Kamboh, U. Ullah, S. Khalid, U. Raza, C. Chakraborty, and F. Al-Turjman, "Path loss modelling at 60 ghz mmwave based on cognitive 3d ray tracing algorithm in 5g," *Peer-to-Peer Networking and Applications*, vol. 14, pp. 3181–3197, 2021.
- [15] R. A. Drebin, L. Carpenter, and P. Hanrahan, "Volume rendering," *ACM Siggraph Computer Graphics*, vol. 22, no. 4, pp. 65–74, 1988.
- [16] B. Mildenhall, P. P. Srinivasan, M. Tancik, J. T. Barron, R. Ramamoorthi, and R. Ng, "Nerf: Representing scenes as neural radiance fields for view synthesis," in *ECCV*, 2020.
- [17] J. T. Barron, B. Mildenhall, M. Tancik, P. Hedman, R. Martin-Brualla, and P. P. Srinivasan, "Mip-nerf: A multiscale representation for anti-aliasing neural radiance fields," in *Proceedings of the IEEE/CVF international conference on computer vision*, pp. 5855–5864, 2021.
- [18] T. Müller, A. Evans, C. Schied, and A. Keller, "Instant neural graphics primitives with a multiresolution hash encoding," *ACM transactions on graphics (TOG)*, vol. 41, no. 4, pp. 1–15, 2022.
- [19] A. Yu, R. Li, M. Tancik, H. Li, R. Ng, and A. Kanazawa, "Plenotrees for real-time rendering of neural radiance fields," in *Proceedings of the IEEE/CVF International Conference on Computer Vision*, pp. 5752–5761, 2021.
- [20] C. Sun, M. Sun, and H.-T. Chen, "Direct voxel grid optimization: Super-fast convergence for radiance fields reconstruction," in *Proceedings of the IEEE/CVF conference on computer vision and pattern recognition*, pp. 5459–5469, 2022.
- [21] A. Chen, Z. Xu, A. Geiger, J. Yu, and H. Su, "Tensorf: Tensorial radiance fields," in *European conference on computer vision*, pp. 333–350, Springer, 2022.
- [22] B. Kerbl, G. Kopanas, T. Leimkühler, and G. Drettakis, "3d gaussian splatting for real-time radiance field rendering," *ACM Transactions on Graphics*, vol. 42, July 2023.
- [23] H. Xie, Z. Chen, F. Hong, and Z. Liu, "Gaussiancity: Generative gaussian splatting for unbounded 3d city generation," *arXiv preprint arXiv:2406.06526*, 2024.
- [24] W. Sun, X. Zhang, F. Wan, Y. Zhou, Y. Li, Q. Ye, and J. Jiao, "Correspondence-guided sfm-free 3d gaussian splatting for nvs," *arXiv preprint arXiv:2408.08723*, 2024.
- [25] G. Wu, T. Yi, J. Fang, L. Xie, X. Zhang, W. Wei, W. Liu, Q. Tian, and X. Wang, "4d gaussian splatting for real-time dynamic scene rendering," in *Proceedings of the IEEE/CVF Conference on Computer Vision and Pattern Recognition*, pp. 20310–20320, 2024.
- [26] Ö. T. Demir, E. Björnson, L. Sanguinetti, et al., "Foundations of user-centric cell-free massive mimo," *Foundations and Trends® in Signal Processing*, vol. 14, no. 3-4, pp. 162–472, 2021.
- [27] R. W. Heath, N. Gonzalez-Prelcic, S. Rangan, W. Roh, and A. M. Sayeed, "An overview of signal processing techniques for millimeter wave mimo systems," *IEEE journal of selected topics in signal processing*, vol. 10, no. 3, pp. 436–453, 2016.
- [28] M. A. Albareem, A. H. Al Habbash, A. M. Abu-Hudrouss, and S. S. Ikki, "Overview of precoding techniques for massive mimo," *IEEE Access*, vol. 9, pp. 60764–60801, 2021.
- [29] F. Liu, Y. Cui, C. Masouros, J. Xu, T. X. Han, Y. C. Eldar, and S. Buzzi, "Integrated sensing and communications: Toward dual-functional wireless networks for 6g and beyond," *IEEE Journal on Selected Areas in Communications*, vol. 40, no. 6, pp. 1728–1767, 2022.
- [30] L. U. Khan, W. Saad, D. Niyato, Z. Han, and C. S. Hong, "Digital-twin-enabled 6g: Vision, architectural trends, and future directions," *IEEE Communications Magazine*, vol. 60, no. 1, pp. 74–80, 2022.
- [31] Y. Lu, X. Huang, K. Zhang, S. Maharjan, and Y. Zhang, "Low-latency federated learning and blockchain for edge association in digital twin empowered 6g networks," *IEEE Transactions on Industrial Informatics*, vol. 17, no. 7, pp. 5098–5107, 2020.
- [32] X. Zhao, Z. An, Q. Pan, and L. Yang, *NeRF2: Neural Radio-Frequency Radiance Fields*. New York, NY, USA: Association for Computing Machinery, 2023.
- [33] R. Zhang, P. Isola, A. A. Efros, E. Shechtman, and O. Wang, "The unreasonable effectiveness of deep features as a perceptual metric," in *Proceedings of the IEEE conference on computer vision and pattern recognition*, pp. 586–595, 2018.
- [34] O. Landron, M. Feuerstein, and T. Rappaport, "A comparison of theoretical and empirical reflection coefficients for typical exterior wall surfaces in a mobile radio environment," *IEEE Transactions on Antennas and Propagation*, vol. 44, no. 3, pp. 341–351, 1996.
- [35] O. Landron, M. J. Feuerstein, and T. S. Rappaport, "In situ microwave reflection coefficient measurements for smooth and rough exterior wall surfaces," in *IEEE 43rd Vehicular Technology Conference*, pp. 77–80, IEEE, 1993.
- [36] V. Degli-Esposti, F. Fuschini, E. M. Vitucci, and G. Falciaesca, "Measurement and modelling of scattering from buildings," *IEEE Transactions on Antennas and Propagation*, vol. 55, no. 1, pp. 143–153, 2007.
- [37] V. M. Patel, J. N. Mait, D. W. Prather, and A. S. Hedden, "Computational millimeter wave imaging: Problems, progress, and prospects," *IEEE Signal Processing Magazine*, vol. 33, no. 5, pp. 109–118, 2016.
- [38] D. Sheen, D. McMakin, and T. Hall, "Three-dimensional millimeter-wave imaging for concealed weapon detection," *IEEE Transactions on Microwave Theory and Techniques*, vol. 49, no. 9, pp. 1581–1592, 2001.
- [39] M. T. Ghasr, S. Kharkovsky, R. Bohnert, B. Hirst, and R. Zoughi, "30 ghz linear high-resolution and rapid millimeter wave imaging system for nde," *IEEE Transactions on Antennas and Propagation*, vol. 61, no. 9, pp. 4733–4740, 2013.
- [40] F. Zhang, C. Wu, B. Wang, and K. R. Liu, "mmeye: Super-resolution millimeter wave imaging," *IEEE Internet of Things Journal*, vol. 8, no. 8, pp. 6995–7008, 2020.

- [41] N. Max, "Optical models for direct volume rendering," *IEEE Transactions on Visualization and Computer Graphics*, vol. 1, no. 2, pp. 99–108, 1995.
- [42] H. L. Van Trees, *Optimum array processing: Part IV of detection, estimation, and modulation theory*. John Wiley & Sons, 2002.
- [43] A. Rose, "The sensitivity performance of the human eye on an absolute scale," *JOSA*, vol. 38, no. 2, pp. 196–208, 1948.
- [44] M. S. Bartlett, "Periodogram analysis and continuous spectra," *Biometrika*, vol. 37, no. 1/2, pp. 1–16, 1950.
- [45] T. Lauer, "Deconvolution with a spatially variant psf," in *Astronomical data analysis II*, vol. 4847, pp. 167–173, SPIE, 2002.
- [46] J. Capon, "High-resolution frequency-wavenumber spectrum analysis," *Proceedings of the IEEE*, vol. 57, no. 8, pp. 1408–1418, 1969.
- [47] J. A. Fessler and A. O. Hero, "Space-alternating generalized expectation-maximization algorithm," *IEEE Transactions on signal processing*, vol. 42, no. 10, pp. 2664–2677, 1994.
- [48] F. A. De Leon and J. J. S. Marciano, "Application of music, esprit and sage algorithms for narrowband signal detection and localization," in *TENCON 2006-2006 IEEE Region 10 Conference*, pp. 1–4, IEEE, 2006.
- [49] P. J. Chung and J. F. Bohme, "Comparative convergence analysis of em and sage algorithms in doa estimation," *IEEE Transactions on Signal Processing*, vol. 49, no. 12, pp. 2940–2949, 2001.
- [50] J. Verhaevert, E. Van Lil, and A. Van de Capelle, "Direction of arrival (doa) parameter estimation with the sage algorithm," *signal processing*, vol. 84, no. 3, pp. 619–629, 2004.
- [51] P. B. Papazian, J.-K. Choi, J. Senic, P. Jeavons, C. Gentile, N. Golmie, R. Sun, D. Novotny, and K. A. Remley, "Calibration of millimeter-wave channel sounders for super-resolution multipath component extraction," in *2016 10th European Conference on Antennas and Propagation (EuCAP)*, pp. 1–5, 2016.
- [52] R. Valenzuela, "A ray tracing approach to predicting indoor wireless transmission," in *IEEE 43rd vehicular technology conference*, pp. 214–218, IEEE, 1993.
- [53] J. W. McKown and R. L. Hamilton, "Ray tracing as a design tool for radio networks," *IEEE Network*, vol. 5, no. 6, pp. 27–30, 1991.
- [54] T. Imai, K. Kitao, and M. Inomata, "Radio propagation prediction model using convolutional neural networks by deep learning," in *2019 13th European Conference on Antennas and Propagation (EuCAP)*, pp. 1–5, IEEE, 2019.
- [55] A. Kamari, Y. Chae, and P. Pathak, "mmsv: mmwave vehicular networking using street view imagery in urban environments," in *Proceedings of the 29th Annual International Conference on Mobile Computing and Networking*, pp. 1–16, 2023.
- [56] R. Levie, Ç. Yapar, G. Kutyniok, and G. Caire, "Radiounet: Fast radio map estimation with convolutional neural networks," *IEEE Transactions on Wireless Communications*, vol. 20, no. 6, pp. 4001–4015, 2021.
- [57] S. Bakirtzis, J. Chen, K. Qiu, J. Zhang, and I. Wassell, "Em deepray: an expedient, generalizable, and realistic data-driven indoor propagation model," *IEEE Transactions on Antennas and Propagation*, vol. 70, no. 6, pp. 4140–4154, 2022.
- [58] G. Cao and Z. Peng, "Raypronet: A neural point field framework for radio propagation modeling in 3d environments," *arXiv preprint arXiv:2406.16907*, 2024.
- [59] C. Gentile, J. Senic, A. Bodi, S. Berweger, R. Caromi, and N. Golmie, "Context-aware channel sounder for ai-assisted radio-frequency channel modeling," in *2024 18th European Conference on Antennas and Propagation (EuCAP)*, pp. 1–5, 2024.
- [60] J. Hoydis, S. Cammerer, F. A. Aoudia, A. Vem, N. Binder, G. Marcus, and A. Keller, "Sionna: An open-source library for next-generation physical layer research," *arXiv preprint arXiv:2203.11854*, 2022.
- [61] J. Hoydis, F. A. Aoudia, S. Cammerer, M. Nimier-David, N. Binder, G. Marcus, and A. Keller, "Sionna rt: Differentiable ray tracing for radio propagation modeling," in *2023 IEEE Globecom Workshops (GC Wkshps)*, pp. 317–321, IEEE, 2023.
- [62] M. Mirza and S. Osindero, "Conditional generative adversarial nets," *arXiv preprint arXiv:1411.1784*, 2014.
- [63] W. Lin and C.-C. J. Kuo, "Perceptual visual quality metrics: A survey," *Journal of visual communication and image representation*, vol. 22, no. 4, pp. 297–312, 2011.
- [64] Y. He, Y. Chen, Y. Hu, and B. Zeng, "Wifi vision: Sensing, recognition, and detection with commodity mimo-ofdm wifi," *IEEE Internet of Things Journal*, vol. 7, no. 9, pp. 8296–8317, 2020.
- [65] Y. Ma, G. Zhou, and S. Wang, "Wifi sensing with channel state information: A survey," *ACM Comput. Surv.*, vol. 52, jun 2019.